Low Complexity Algorithm for Range-Point Migration-Based Human Body Imaging for Multistatic UWB Radars

Yoshiki Akiyama, and Shouhei Kidera ⬚, *Member, IEEE*

Abstract—**High-resolution, short-range sensors that can be applied in optically challenging environments (e.g., in the presence of clouds, fog, and/or dark smog) are in high demand for various applications. Ultrawideband radar is a promising sensor that is suitable for short-range surveillance or watching sensors. Range-point migration (RPM) has been recently established as a promising imaging approach to achieve accurate and real-time 3-D imaging. However, when objects with many scattering points are dealt with, such as a human body, RPM suffers from high computational costs. In this letter, we propose an algorithm with a lower complexity for an RPM-based 3-D imaging method by introducing a sampling-based scattering center extraction with a simplified evaluation function, in which an efficient sample pattern is provided by a golden ratio. The results from a finite-difference time-domain-based numerical test, which introduces a realistic human body object, demonstrate that our proposed method remarkably reduces the computational cost without sacrificing the reconstruction accuracy.**

Index Terms—**3-D imaging, multistatic observation model, range-point migration (RPM), short-range sensor, ultrawideband (UWB) radar.**

I. INTRODUCTION

ULTRAWIDEBAND (UWB) radars offer significant advantages, such as higher range resolution and applicability to optically harsh environments (e.g., dense fog, dusty air, or through-the-wall conditions). The above-mentioned advantages form the basis for various short-range sensing applications such as human body detection in visually blurred or through-the-wall scenarios and observation sensors that address the privacy issues of elderly or disabled persons living alone. Various studies have been conducted on 3-D imaging methods that focus on short-range radars. The major approaches in 3-D imaging are primarily based on the delay-and-sum (DAS) algorithms, such as synthetic aperture radar [1], Kirchhoff migration approaches [2], the diffraction tomography (DT) method [3], or compressed sensing (CS)-based approaches [4] However, DAS-based methods usually require a high computational cost to obtain a full 3-D image, and they suffer from inaccuracies in the

reconstructions of objects with continuous boundaries (not pointwise shapes), that are located close to the sensors. The fast DT algorithm [3] achieves a real-time 3-D imaging by the fast Fourier transform-based acceleration on the 2-D array data. However, it requires a data interpolation process in the wavenumber domains, and a coarse array configuration can come up with an ambiguous image. In addition, while the CS-based method avoids the ambiguity responses due to a grating lobe, and obtains a higher resolution image, it often requires a numerical solution for large-scale optimization problems, thus, incurring an extremely expensive computational cost to obtain a full 3-D image.

As a promising solution to the above-mentioned problem, the range-point migration (RPM) method has been developed, which offers several advantages in terms of accuracy and low computational complexity in 3-D imaging. It is also acceptable for coarse-array data resulting from an incoherent process. This method is based on the batch conversion algorithm from range point (RP), which is defined as a set of each observed time delay and antenna location, to a corresponding scattering center point [5]. The notable feature of this method is its effective solution to the joint problem between the range and the direction of arrival (DOA) using a Gaussian kernel-based DOA estimator. Furthermore, it is free from complicated pre-processing for connecting or paring RPs. A number of studies have demonstrated the effectiveness of this method in different observation models, where it achieves a higher reconstruction accuracy even in cases with high interference [6], [7]. In particular, Sasaki *et al.* [7] deal with the imaging issue of a human body by exploiting micro-Doppler discrimination to enhance the accuracy and computational efficacy of the RPM. Nonetheless, the RPM still suffers from an inherent problem in which the computational complexity of the original RPM algorithm drastically increases according to the number of RPs, because it requires the calculation of the intersection points of three spheroids for all possible combinations of the measured RPs.

In order to avoid an explosive increase in the computational cost in the original RPM, in this letter, we introduce a sampled-point extraction algorithm for which the basic idea was recently proposed in [8]. First, this method retains a number of discrete points, which are sampled on an assumed spheroid obtained by each RP. Then, the scattering center is extracted from these sampled points and not from the intersection points. In addition, this method adopts the golden ratio sampling
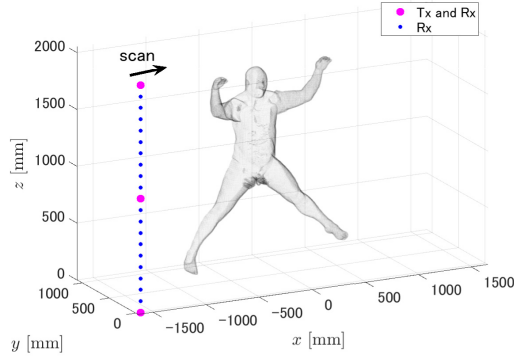
Fig. 1.   Observation model assuming the 1-D MIMO array with linear scanning.

pattern as one of the most effective spatial patterns with the least gaps. In order to make the scheme suitable, this method further introduces a simplified evaluation function for a Gaussian kernel estimator, which requires a much less computational complexity cost, even for a multistatic observation model. The finite-difference time-domain (FDTD)-based 3-D numerical simulations, which use a realistic human body dielectric phantom, demonstrate that the proposed method remarkably reduces the computational cost compared *with* the original RPM method without sacrificing the reconstruction accuracy.

II. OBSERVATION MODEL

Fig. 1 shows the observation model. The 1-D array, which assumes a multiple-input multiple-output (MIMO) radar, along the z-axis is scanned in the x-direction. The locations of the transmitting and receiving antenna elements are defined as $L_T = (X_T, 0, Z_T)$ and $L_R = (X_R, 0, Z_R)$, respectively. For each L_T and L_R combination, the recorded electric field is denoted as $s'(L_T, L_R, t)$, where t denotes a fast time. $s(L_T, L_R, t)$ denotes the output of the range extraction filter of $s'(L_T, L_R, t)$. $s(L_T, L_R, t)$ is converted into $s(L_T, L_R, R)$, with $R' = ct/2$ using radio-wave speed c. $q \equiv (L_T, L_R, R)$ is defined as the RP, which is extracted from the local maxima of L_T, L_R with respect to R.

III. CONVENTIONAL IMAGING METHODS

A. DAS-Based Method

Many studies on short-range radar imaging have been conducted on the basis of the DAS approach, which is known as SAR processing or multidimensional beamforming. Even though the DAS-based methods provide noise robust and accurate images, when a target is expressed as an aggregation of points, they cannot offer a sufficient accuracy for continuous boundaries because the DAS algorithm assumes that the scattering point is invariant with respect to the observation point, which is valid for a point-shaped target. Conversely, in the case of a continuous-shaped boundary, the dominant scattering center moves along its boundary and the above-mentioned DAS method assumption or principle is invalid and yields an inaccuracy in the shape estimation. Furthermore, the complex-value-based DAS method requires dense sampling intervals

(within half the wavelength of the dielectric medium) between the observation points in order to avoid the grating lobe effect.

B. RPM-Based Method

The RPM method has been demonstrated to address the aforementioned issue when introducing an RP conversion algorithm with a Gaussian kernel estimator is introduced. According to the geometric optics approximation, one scattering center point on the target boundary that corresponds to one RP q should exist on a spheroid with focal points L_T and L_R and major radius R. In order to extract the scattering center point, this method is used to calculate all the possible intersection points determined by other RPs (called SubRPs). Then, the RP determines the scattering center $\hat{p}(q_i)$ that corresponds to the RP (called MainRP) q_i, such that

$$\hat{p}(q_i) = \underset{p^{\text{int}}(q_i; q_l, q_m) \in \mathcal{P}_i}{\arg \max} \sum_{(q_j, q_k) \in \mathcal{Q}_{\text{all}}} g(q_i; q_j, q_k)$$
$$\times \exp\left\{ -\frac{\|p^{\text{int}}(q_i; q_j, q_k) - p^{\text{int}}(q_i; q_l, q_m)\|}{2\sigma_r^2} \right\}. \tag{1}$$

Here, $p^{\text{int}}(q_i; q_j, q_k)$ denotes the intersection points between the three spheroids that are determined by the RPs q_i, q_j, and q_k, respectively. $\mathcal{P}_i$ denotes a set of these intersection points, and σ_r is determined by considering the spatial density of the accumulated intersection points. $\mathcal{Q}_{\text{all}}$ denotes the set of all RPs. The weighting function $g(q_i; q_j, q_k)$ is defined as

$$g(q_i; q_j, q_k) = s(q_j)\exp\left\{ -\frac{D(q_i, q_j)}{2\sigma_D^2} \right\}$$
$$+ s(q_k) \exp\left\{ -\frac{D(q_i, q_k)}{2\sigma_D^2} \right\} \tag{2}$$

where σ_D is empirically determined. $D(q_i, q_j)$ denotes the actual separation of the two sets of transmitting and receiving antennas such that

$$D(q_i, q_j) = \min(\|L_{T,i} - L_{T,j}\|^2 + \|L_{R,i} - L_{R,j}\|^2$$
$$\times \|L_{T,i} - L_{R,j}\|^2 + \|L_{R,i} - L_{T,j}\|^2). \tag{3}$$

The terms $\exp(-\|D(q_i, q_j)\|^2/2\sigma_D^2)$ and $\exp(-\|D(q_i, q_k)\|^2/2\sigma_D^2)$ in (2) denote the weight function, based on the characteristic determined in which the intersection point of $p^{\text{int}}(q_i; q_j, q_k)$ should converge to the actual scattering center when $L_{T,j}, L_{T,k} \to L_{T,i}$ (also in L_R), as detailed in [5]. Thus, σ_D should be determined to be greater than the minimum array or scanning interval.

We note that, in (1), the optimal combination of q_l and q_m is determined by a full search for all possible combinations. A number of studies demonstrated that the RPM achieves accurate and high-speed 3-D imaging even with an elaborate target shape, which generates a richly interfered situation, by avoiding the preconnection procedure of the RPs. However, when dealing with an object with many scattering points, such as a human body, the RPM suffers from an explosive increase in the computational cost because of the large number of intersection points in the three spheroids that must all be
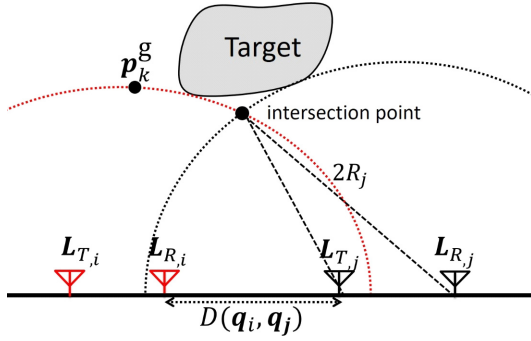
Fig. 2. Relationship between sample point as $p_{k,i}^g$ and intersection point.

Fig. 3. Relationship between sampling point and transmitting and receiving antennas.

numerically solved. In a quantitative manner, the computational complexity of the original RPM method is estimated to be $O(N^5)$, where N denotes the number of available RPs.

IV. PROPOSED RPM ALGORITHM

In order to achieve a substantial reduction in the computational complexity of the RPM method, in this letter, we introduce a sample-point extraction-based algorithm to avoid the calculation of the intersection point of the spheroids, for which the basic idea was introduced in [8]. To obtain further acceleration, in this letter, we modify the evaluation function in (1), to make it suitable for the sampled-point extraction scheme. The proposed idea focuses on the fact that the interval of the azimuth angle from the intersection points to the sample point on the assumed spheroid is almost proportional to the distance defined as

$$L(p_{i,k}^g, q_j) \equiv \left| \|L_{T,j} - p_{i,k}^g\| + \|L_{R,j} - p_{i,k}^g\| - 2R_j \right|/2. \tag{4}$$

Here, in the 3-D model, $p_{i,k}^g$ denotes the kth sampled point on the spheroid obtained from q_i, for which the focal points are $(L_{T,i}, L_{R,i})$ and the major radius is R_i. By exploiting (4), this algorithm determines the scattering center $p(q_i)$ as

$$\hat{p}(q_i) = \arg\max_{p_{i,k}^g} \sum_{q_j \in Q_i} s(q_j) \exp\left\{ -\frac{D(q_i, q_j)^2}{2\sigma_D^2} \right\}$$
$$\times \exp\left\{ -\frac{L(p_{i,k}^g, q_j)^2}{2\sigma_L^2} \right\} \tag{5}$$

where $D(q_i, q_j)$ is defined in (3), and σ_D and σ_L are the constant parameters. Since σ_L expresses the spatial variations of the intersection points, it is usually set to a sufficiently smaller value than the array interval. Fig. 2 shows the relationship between the sample point and the intersection points. Compared with (1) in the original RPM, (5) offers a univariate optimization problem and does not require the combined summation in calculating the evaluation function, which considerably reduces the computational complexity. In addition, the computational cost of this method does not significantly depend on the number of processed RPs (i.e., N), which is proportional to the number of objects. Here, we note that the computational complexity of this method is estimated to be $O(MN^2)$, where M denotes the total number of sample points.
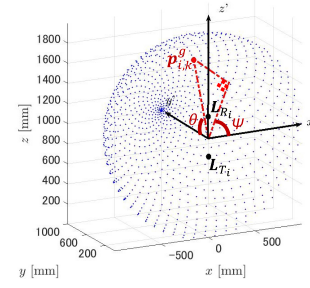
However, the accuracy of the proposed method naturally depends on the spatial interval or the pattern of the sample points, which should be preliminarily given. In this letter, we introduce a golden ratio-based pattern, which occurs in some patterns in nature, such as the spinal arrangement of leaves, as the most efficient pattern for these sample points without gaps. Here, we introduce the parameters θ and ψ as the azimuth and elevation angles of the spheroid, respectively, as shown in Fig. 3. Each sample point on the golden ratio pattern of q_i is expressed as follows:

$$p_{i,k}^g = (L_{T,j} + L_{R,j})/2 + R_i(\sin\theta_k \cos\psi_k, \cos\theta_k, \sin\theta_k \sin\psi_k) \tag{6}$$

where the following relationship holds:

$$\theta_k = (k-1)\pi/2M \tag{7}$$
$$\psi_k = 4(k-1)\pi/M(1+\sqrt{5}). \tag{8}$$

The actual procedure of the proposed method is described as follows:

Step 1: Signals are recorded at each combination of transmitting and receiving antennas as $s(L_T, L_R, t)$, and are processed by the range extraction filter, whose output is denoted as $s(L_T, L_R, R')$.

Step 2: RPs are extracted as q_i from the local maxima of $s(L_T, L_R, R')$ with respect to R'.

Step 3: For each RP q_i, the sampling points on the spheroid are created using (6) as $p_{i,k}^g$.

Step 4: $\hat{p}(q_i)$ is determined by (6).

Step 5: Steps 3) and 4) are processed for all RPs, and the target boundary points are expressed as an aggregation of scattering center points $\hat{p}(q_i)$.

V. EVALUATION IN NUMERICAL SIMULATION

In this section, we describe the performance evaluation of each method on a realistic human body phantom using the 3-D FDTD-based numerical simulations. Here, the transmitted signal forms a pulse-modulated signal, with a center frequency of 5.0 GHz and a bandwidth of 2.0 GHz. An elaborate human model is investigated as an object as shown in Fig. 1, which is implemented in the commercial software XFdtd Bio-Pro, where each tissue has a realistic dielectric property [9]. Here, in order to obtain a higher range resolution using the RPs extraction scheme, the Capon filter is adopted,
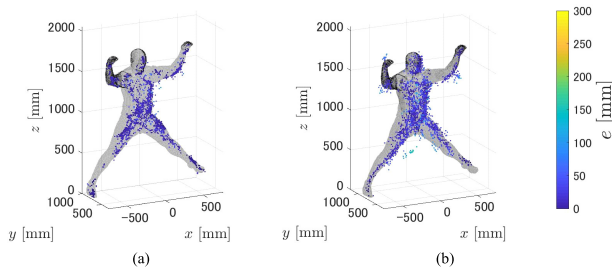
Fig. 4.   3-D reconstruction results. Color: reconstruction error e. (a) Original RPM. (b) Proposed method.
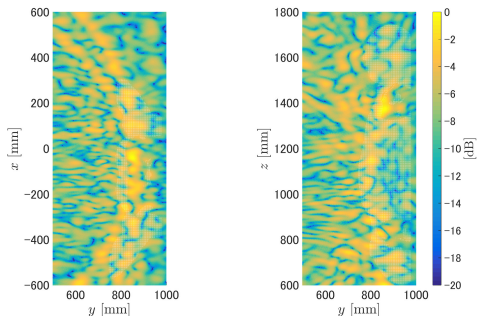
Fig. 5.   Sectional view of reconstruction results obtained by the DAS method. (a) $x = 0$ mm. (b) $z = 1300$ mm. White dots: actual human body shape.

TABLE I

COMPARISON FOR COMPUTATIONAL COMPLEXITY
AND ACTUAL PROCESSING TIMES

	Original RPM	Proposed RPM
Computational complexity	$O(N^5)$	$O(MN^2)$
Processing times	6.0×10^5 sec	410 sec
Quantities	$N = 3053$	$N = 3053$ $M = 5000$

whose effectiveness been well demonstrated in [10]. The 1-D linear array antennas are composed of 3 transmitting antennas and 21 receiving antennas, where the separation of the transmitting and receiving antennas is 1000 and 100 mm, respectively. This array antenna is scanned along the x-axis for -1600 mm $\leq x \leq 1600$ mm with a 200-mm sampling interval. Fig. 4 shows the reconstruction results obtained by the original RPM (intersection point based) and the proposed RPM methods. Here, the numbers of processed RPs and sampling points in the proposed method are $N = 3053$ and $M = 5000$, respectively. These figures show that both the original and the proposed RPM methods accurately reconstruct each part of the human body. In order to quantitatively analyze the reconstruction image, the reconstruction error, denoted as e is introduced as the minimum distance between the actual target boundary and each reconstructed point. The accumulation proportions that satisfy $e \leq 10$ cm are 100% (2105/2105) for the original RPM method and 98.1% (2705/2804) for the proposed method, respectively. Table I lists the comparison of the computational complexity and the actual processing times of each method. We note that the calculation time is more than 6×10^5 s (approximately 165 h) for the original RPM method and 410 s for the proposed method using an Intel(R) Xeon(R) CPU E5-2680 v4 at 2.40 GHz and 128-GB RAM.
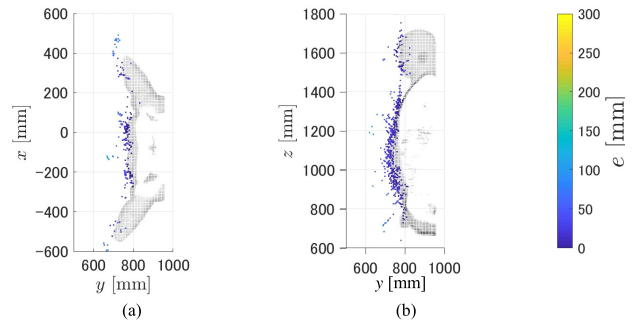
Fig. 6.   Sliced view of reconstruction results obtained by the proposed method. Black dots: actual human body shape. (a) 1250 mm $\leq z \leq$ 1350 mm. (b) -50 mm $\leq x \leq$ 50 mm.
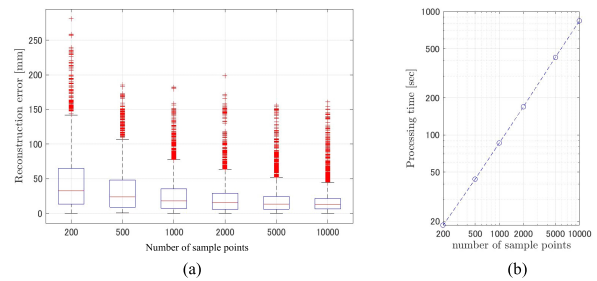
Fig. 7.   (a) Box-plot diagram for reconstruction error e versus the number of sample points (M). (b) Processing time versus the number of sample points (M).

In other words, approximately 1400-fold times acceleration can be achieved with the proposed method, without sacrificing the reconstruction accuracy. For reference, Fig. 5 shows the image obtained by the DAS algorithm, whereas Fig. 6 shows a sliced view of the reconstruction results by the proposed method, for comparison. Fig. 5 shows that the DAS image does not present a significant boundary shape of the human body, compared with that obtained by the proposed method as shown in Fig. 6.

Note that the accuracy of the proposed method naturally depends on the number of sampling points (i.e., the density of the sampling pattern). Hence, we predict that the increase in the sampling points incurs a high computational cost. Here, in order to quantitatively assess the aforementioned characteristic, we investigated the reconstruction performance under different numbers of sampling points. Fig. 7 shows the box-plot diagram of error e assuming the same model as that shown in Fig. 1 and the required computational time for each number of sampling points. These figures show that lower limits exist for reconstruction accuracy e, as shown in Fig. 7(a), and the computational costs are approximately linear with the number of sampling points, which is also another advantage of the proposed algorithm.

Next, the robustness of the proposed method to additive noise is investigated, where a white Gaussian noise is added to each recorded electric field. Fig. 8 shows the reconstruction results by the proposed method, where the average signal-to-noise ratio (SNR) is 20 dB, assuming the same model shown in Fig. 1. Fig. 8 shows that the proposed method has a significant robustness to additive noise, even with the
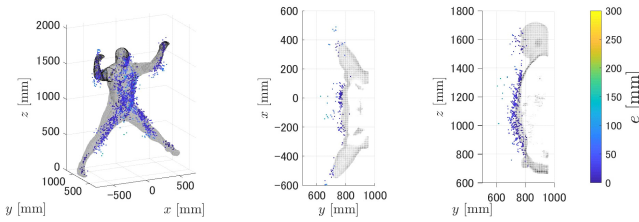
Fig. 8.   3-D reconstruction results obtained by the proposed method at 20-dB SNR.

TABLE II
QUANTITATIVE COMPARISON FOR EACH SNR LEVEL
IN THE PROPOSED METHOD

SNR	RMSE	Cumulative probability for $e \leq 10$ cm
∞	22.5 mm	98.1 %
30 dB	22.6 mm	98.6 %
20 dB	22.3 mm	98.7 %
10 dB	56.1 mm	92.5 %

TABLE III
QUANTITATIVE COMPARISON FOR EACH SNR LEVEL
IN THE PROPOSED METHOD

(σ_D, σ_L)	RMSE	Cumulative probability for $e \leq 10$ cm
(1000mm, 20 mm)	22.5 mm	98.1 %
(1500mm, 20 mm)	24.8 mm	97.3 %
(500mm, 20 mm)	35.7 mm	94.4 %
(1000mm, 10 mm)	20.4 mm	98.8 %
(1000mm, 30 mm)	26.4 mm	97.2 %

use of the Capon filter. Table II summarizes the results for different SNR levels. The proposed method maintains noise robustness similar to that of the original RPM method, in which both the original and the proposed methods apply false-image reduction by considering the quantity of the evaluation function in (5) at the postprocessing.

Finally, the sensitivity study of the parameters used in the proposed method, namely, σ_D and σ_L, assuming the same model shown in Fig. 1 is investigated next. Table III summarizes the quantitative analysis under each parameter variation and shows that no severe sensitivity to the selected parameters exists, especially for σ_L. In contrast, we confirmed that when σ_D becomes smaller, the error becomes relatively larger, especially along the z axis, because the minimum separation of the transmitting antennas along the z-axis is 1000 mm. Thus, we recommend that σ_D should be larger than the minimum separation for both the transmitting and receiving antennas.

VI. CONCLUSION

In this letter, we proposed a considerably lower complexity algorithm for 3-D image reconstruction with the RPM method using a sample-point-based scattering center extraction, in which a golden ratio sampling pattern and a simplified evaluation function are introduced to upgrade the computational efficacy. The results from the FDTD-based numerical simulations, using a realistic human body model, demonstrate that our proposed RPM method significantly accelerates the computational speed without sacrificing the reconstruction accuracy, compared with the original RPM method. We note that one of the advantages of the UWB radar is its applicability to through-the-wall imaging (TWI) scenario, and this algorithm can be extended to a TWI model using the suitable modifications by considering the distorted propagation model similar to that in [11].

REFERENCES

[1] T. C. Chen, J. H. Liu, P. Y. Chao, and P. C. Li, "Ultrawideband synthetic aperture radar for respiratory motion detection," *IEEE Trans. Geosci. Remote Sens.*, vol. 53, no. 7, pp. 3749–3763, Jul. 2015.

[2] F. Soldovieri, A. Brancaccio, G. Prisco, G. Leone, and R. Pierri, "A Kirchhoff-based shape reconstruction algorithm for the multimonostatic configuration: The realistic case of buried pipes," *IEEE Trans. Geosci. Remote Sens.*, vol. 46, no. 10, pp. 3031–3038, Oct. 2008.

[3] W. Zhang and A. Hoorfar, "Three-dimensional real-time through-the-wall radar imaging with diffraction tomographic algorithm," *IEEE Trans. Geosci. Remote Sens.*, vol. 51, no. 7, pp. 4155–4163, Jul. 2013.

[4] S. Ram and A. Majumdar, "High-resolution radar imaging of moving humans using Doppler processing and compressed sensing," *IEEE Trans. Aerosp. Electron. Syst.*, vol. 51, no. 2, pp. 1279–1287, Apr. 2015.

[5] S. Kidera, T. Sakamoto, and T. Sato, "Accurate UWB radar 3-D imaging algorithm for complex boundary without wavefront connection," *IEEE Trans. Geosci. Remote Sens.*, vol. 48, no. 4, pp. 1993–2004, Apr. 2010.

[6] T. Sakamoto, T. Sato, P. Aubry, and A. Yarovoy, "Fast imaging method for security systems using ultrawideband radar," *IEEE Trans. Aerosp. Electron. Syst.*, vol. 52, no. 2, pp. 658–670, Apr. 2016.

[7] Y. Sasaki, F. Shang, S. Kidera, T. Kirimoto, K. Saho, and T. Sato, "Three-dimentional imaging method incorporating range points migration and Doppler velocity estimation for UWB millimeter-wave radar," *IEEE Geosci. Remote Sens. Lett.*, vol. 14, no. 1, pp. 122–126, Dec. 2016.

[8] Y. Akiyama and S. Kidera, "Acceleration for RPM-based three-dimensional imaging for 140 GHz-band millimeter wave radar," in *Proc. IEEE Int. Symp. Antenna Propag. (ISAP)*, Nov. 2017, pp. 1–2.

[9] C. Gabriel, "Compilation of the dielectric properties of body tissues at RF and microwave frequencies," Air Force Materiel Command, Brooks Air Force Base, San Antonio, TX, USA, Tech. Rep. AL/OE-TR-1996-0037, 1996.

[10] S. Kidera, T. Sakamoto, and T. Sato, "Super-resolution UWB radar imaging algorithm based on extended capon with reference signal optimization," *IEEE Trans. Antennas Propag.*, vol. 59, no. 5, pp. 1606–1615, May 2011.

[11] S. Kidera, C. Gao, T. Taniguchi, and T. Kirimoto, "Ellipse based image extrapolation method with RPM imaging for through-the-wall UWB radar," in *Proc. IEEE Geosci. Remote Sens. Symp.*, Jul. 2015, pp. 385–388.